



Friction and chaos: Influence of the damping coefficient on atomic-scale stick-slip on hexagonal crystal lattices

Enrico Gnecco ^{1,*}, Liron Agmon,² and Ronen Berkovich ^{2,3}

¹Marian Smoluchowski Institute of Physics, Jagiellonian University, Lojasiewicza 11, 30-348 Krakow, Poland

²Department of Chemical Engineering, Ben-Gurion University of the Negev, Beer-Sheva 8410501, Israel

³The Ilze Katz Institute for Nanoscience and Technology, Ben-Gurion University of the Negev, Beer-Sheva 8410501, Israel



(Received 14 January 2022; revised 2 June 2022; accepted 2 June 2022; published 21 June 2022)

We have numerically investigated the occurrence of long slips when a point mass representing a tip of a solid surface is elastically driven on a hexagonal surface lattice along an arbitrary direction. Tip pathways and slip length histograms are estimated for different values of the damping coefficient γ defining the duration of the slip phases. The results are compared with a map of all possible “slip channels” as obtained analytically with the Prandtl-Tomlinson model in two dimensions. The histograms of the corresponding force drops obtained for different values of γ could be directly compared with experimental data obtained by friction force microscopy, which would allow us to quantify the energy dissipation in the slip phase in different loading conditions and shed light on quantum effects (phonon and/or electron-hole generation) accompanying sliding friction on the atomic scale.

DOI: [10.1103/PhysRevB.105.235427](https://doi.org/10.1103/PhysRevB.105.235427)

I. INTRODUCTION

The damping coefficient γ smoothing the oscillations of a sharp tip sliding on a solid surface is one of the most elusive parameters to characterize experimentally. If the sliding occurs in a vacuum, γ is related to the excitation of phonons and possibly of electrons, both of which propagate from the contact area into the bulk [1–3]. In a humid environment, the situation is complicated by the viscous and electronic properties of the surrounding liquid. A direct estimation of γ from the duration of the slip phases is difficult even using fast controllers (3 MHz bandwidth) in atomic force microscopy (AFM) measurements under ultrahigh vacuum (UHV) conditions [4]. Nevertheless, indirect information on γ can be obtained from the distribution of the lateral force variations or, equivalently, of the slip lengths [5–12]. In dry conditions, the average slip length Δx tends to increase by increasing the normal force or, more precisely, the value of the parameter $\eta = 4\pi^2 U_0 / (ka^2)$, where U_0 and a are, respectively, the amplitude and the periodicity of the potential, and k is the spring constant [9,13]. Alternatively, Δx increases if the driving velocity V decreases [5] or the damping coefficient γ determining the energy dissipation rate in the slip phase decreases [8]. The last two possibilities are not equivalent since the parameters V and γ do not appear on equal footing in the equation of motion, see below. Note also that the environmental conditions can introduce a nontrivial dependence of γ on the loading conditions [14–16], but this issue is not considered in the present work.

In [8] the combined influence of the parameter γ and the temperature T was studied numerically in one dimension

(1D). Here we extend the analysis to two dimensions (2D) on the important example of hexagonal lattices [17]. Histograms of the slip length for different lattice orientations of the crystal lattice are presented and compared to the tip trajectories in the phase space for a given value of η where stick-slip is fully established in overdamped conditions, and for different values of γ , with special focus on two cases corresponding to critically damped and underdamped oscillations. Not so surprisingly, the complexity of the problem is considerably increased, as compared to 1D, by the presence of several slip channels with a broad distribution of orientations.

II. MODEL

We consider the tip motion in a hexagonal energy landscape:

$$U_{\text{int}}(x, y) = -U_0 \left(2 \cos \frac{2\pi x}{a} \cos \frac{2\pi y}{a\sqrt{3}} + \cos \frac{4\pi y}{a\sqrt{3}} \right). \quad (1)$$

The spring support is driven over a length of 200 nm along a direction forming a given angle α with respect to the x axis with a velocity $V = 25$ nm/s. The corresponding equation of motion

$$m\dot{\mathbf{v}} + m\gamma\mathbf{v} + \nabla U_{\text{int}} + k(\mathbf{r} - \mathbf{V}t) = \xi(t) \quad (2)$$

has been solved numerically for $a = 0.246$ nm (corresponding to the lattice constant of HOPG), and a tip mass $m = 5 \times 10^{-11}$ kg. The vector \mathbf{r} denotes the tip position on the x - y plane, $\mathbf{v} = \dot{\mathbf{r}}$ is the tip velocity, and \mathbf{V} is the driving velocity. The spring constant is supposed to take the same value $k = 1$ N/m in both x and y directions, as usually observed in lattice-resolved AFM friction measurements in UHV [18]. The critical value of γ distinguishing between overdamped and underdamped oscillations in the slip phase is defined as

*Correspondence should be addressed to enrico.gnecco@uj.edu.pl

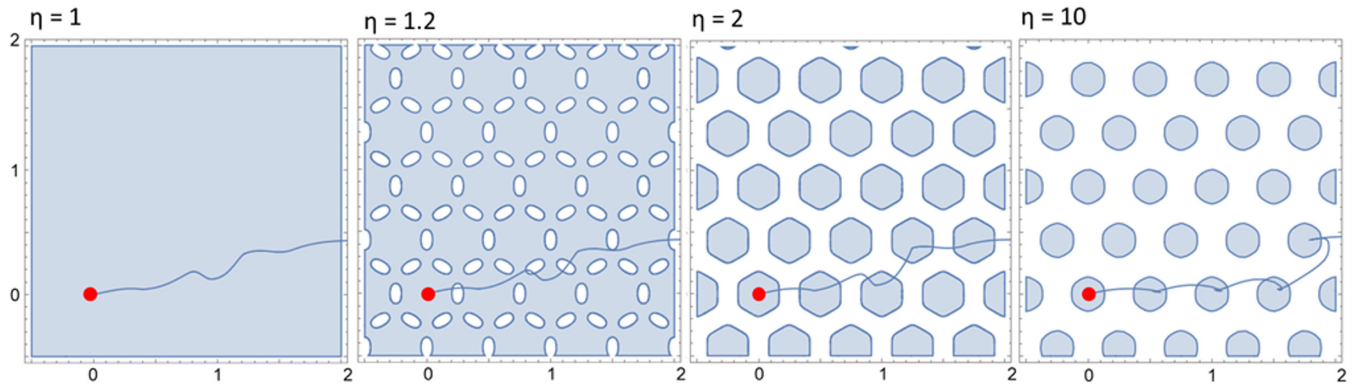


FIG. 1. Stability regions and tip pathways in the xy plane corresponding to increasing values of the parameter η defined in the text. The tip is pulled under overdamped conditions at an angle of $\alpha = 12^\circ$ starting from the red dot. The length unit is defined by the lattice constant a .

$\gamma_c = 2\sqrt{k/m}$. Thermal vibrations are introduced by means of a random noise function $\xi(t)$ satisfying the fluctuation-dissipation theorem: $\langle \xi(t)\xi(t') \rangle = 2m\gamma k_B T$, where k_B is the Boltzmann's constant, and T is the temperature. In the following, the Langevin equation (2) is solved by means of the Ermak algorithm [19] with a time step $\Delta t = 10^{-8}$ s. From the coordinate x of the tip as a function of time t , the component of the spring force along the x axis is obtained as $F_x = k(Vt - x)$.

At $T = 0$ we define the onset of the slip phase by the condition that the spring elongation, or, equivalently, the spring force F starts to decrease. This approximation is accurate for sufficiently large values of η . If $T \neq 0$ this definition is not applicable, due to thermal vibrations. In this case we assume that the slip starts when the difference between the actual value of F_x and the value recorded after a time $\Delta t = 30 \mu\text{s}$ is above a certain threshold $\Delta F_{\text{th}} = 0.1 \text{ nN}$ (these values turn out to be adequate for the time evolution of the spring force reported below). The estimation of the force variation accompanying a slip is made difficult by the tip oscillations concluding the slip phase. Here this quantity is calculated (for the i th slip) as

$$\Delta F_i = F_{i+1} - F_i + \frac{\eta}{\eta + 1} k \Delta X_i, \quad (3)$$

where F_i is the lateral force at the slip onset, ΔX_i is the distance between the minimum in the $F(X)$ curve corresponding to the shot point and the next one, and η is the parameter introduced previously. The corrective factor in front of k in Eq. (3) accounts for the difference between the average value of $|F'(X)|$ and k , as discussed in [20] based on the Prandtl-Tomlinson model in 1D.

III. RESULTS AND DISCUSSION

A. Allowed transitions

In 1D the occurrence of slips corresponding to n lattice constants becomes possible under overdamped conditions, at well-defined values of the parameter η . These values are given by the solutions of the equation $f(\eta) \equiv \sqrt{\eta^2 - 1} + \arccos(-1/\eta) = n\pi$ corresponding to $n = 1, 2, 3, \dots$ and they are equal to 1, 4.603, 7.790, ... [8, 13, 21]. In 2D the situation is much more complex [22]. On the hexagonal potential defined by Eq. (1) stick-slip is again possible only if $\eta >$

1. If η is increased up to 1.454 the stability region on the x - y plane breaks apart into two lattices of large and small patches with approximately hexagonal and triangular shapes. If η increases further the triangular patches shrink, and they completely disappear when $\eta = 2$. The remaining hexagonal patches become more and more round shaped as $\eta \rightarrow \infty$. The limit shape is approximately a circle with radius $R = a/4$, as demonstrated in [22]. In Fig. 1 the breaking up of the regions of stability is illustrated for different values of η between 1 and 10. Note also how the tip path, as estimated numerically (with $\alpha = 12^\circ$ and $T = 0$), evolves from a continuous curve to a series of wavy segments connecting consecutive pinning points on the lattice. As also shown in [22], the path inside the stability regions is described by the implicit equation

$$\tan \alpha = \frac{\sqrt{3}y + \eta \sin \frac{y}{\sqrt{3}} \left(\cos x + 2 \cos \frac{y}{\sqrt{3}} \right)}{\sqrt{3} \left(x + \eta \sin x \cos \frac{y}{\sqrt{3}} \right)} \quad (4)$$

[with $a/(2\pi)$ as length unit].

The “landing points” (x, y) where the slips can end are given by the solutions of the equation $\nabla(U_{\text{int}} + U_{\text{el}}) = 0$ located inside the stability regions, where $U_{\text{el}}(x, y; t) = (k/2)(\mathbf{r} - \mathbf{V}t)^2$ is the variable elastic potential associated with the spring elongation. The landing points can be estimated for the very first slip observing that, due to the quasi-isotropy of static friction on the hexagonal potential [22], the time t_c when the equilibrium becomes unstable is approximately given by $vt_c = (a/2\pi)f(\eta)$, as in 1D. Substituting the expression for the potential (1), one gets

$$\begin{aligned} \frac{2\pi x}{a} - f(\eta) \cos \alpha + \eta \sin \frac{2\pi x}{a} \cos \frac{2\pi y}{\sqrt{3}a} &= 0, \\ \frac{2\pi y}{a} - f(\eta) \sin \alpha + \frac{\eta}{\sqrt{3}} \sin \frac{2\pi y}{\sqrt{3}a} \left(\cos \frac{2\pi x}{a} + 2 \cos \frac{2\pi y}{\sqrt{3}a} \right) &= 0. \end{aligned} \quad (5)$$

We have solved Eq. (5) for $\eta = 10$ and $\alpha = 0^\circ, 12^\circ$, and 30° and estimated 11, 13, and 12 possible landing points, as shown in Figs. 2(a)–2(c). Slight deviations from this “attractor pattern” are expected in the subsequent slips, when the tip position is initially offset with respect to the scan line [23] and additional locations may become accessible. The corresponding slips have been marked in Fig. 2(b), numbered from

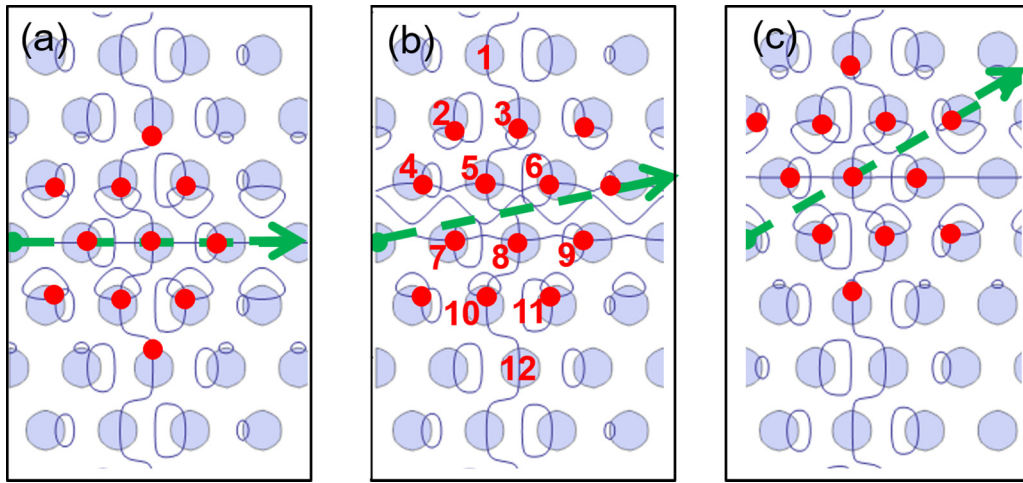


FIG. 2. Landing points (red dots) theoretically accessible by a point mass shot from the green dots at the angles (a) $\alpha = 0^\circ$, (b) $\alpha = 12^\circ$, and (c) $\alpha = 30^\circ$ over the stability region patches (light purple) when the stick-slip parameter $\eta = 10$.

1 to 12. Note that the sites 1 and 12 are not present. Their lack of appearance is due to the aforementioned offset of the tip coordinate with respect to the scan direction (x axis).

B. Influence of damping coefficient and moderate thermal effects

In the following, the pulling direction is kept fixed at an angle $\alpha = 12^\circ$ with the x axis. Figures 3(a) and 3(d) show the beginning of the tip path at $T = 0$ K with $\eta = 10$. The tip oscillations are either critically damped ($\gamma = \gamma_c$) or underdamped ($\gamma = 0.1\gamma_c$). The corresponding attractor patterns, as estimated from the entire tip path, are shown in Figs. 3(b) and 3(e). Here the attractors are simply represented by blue dots. The position of each one is defined by the change of the tip coordinates Δx and Δy , occurring in a jump, and numbered according to the scheme in Fig. 2(b). In the first case, the three landing points (4, 5, and 7) are close to the shot point. The situation is more complex if the damping coefficient is lowered to $0.1\gamma_c$. In this case many more locations become accessible [Fig. 3(e)], but as seen from the tip path in Fig. 3(d), not all landing attempts are concluded successfully. We have also plotted the statistical distribution of the horizontal tip shift during the slip, Δx ($\neq \Delta X$), see Figs. 3(c) and 3(f). In both cases, single slips with small deviation from the scan direction (type 7) are the most common. Interestingly, when $\gamma = 0.1\gamma_c$, triple slips with the same orientation (type 9) are much more frequent than double slips (type 8).

In the presence of thermal vibrations, slip events become thermally activated [24]. If $\gamma = \gamma_c$ the long jumps of type 5 observed at 0 K tend to be replaced by two single slips 4 and 7, as seen in Figs. 3(g) and 3(h) for $T = 70$ K. In the Δx distribution all peaks are lowered and broadened, and the third peak (5) almost disappears [Fig. 3(i)]. Similarly, if $\gamma = 0.1\gamma_c$, most of the longer slips observed at 0 K are suppressed [Figs. 3(j) and 3(k)]. The peak distribution is again lowered and broadened, and only slips 7 and 8 remain distinguishable in the histogram [Fig. 3(l)]. Figure 4 shows the corresponding time evolution of the lateral force F_x and the statistical dis-

tribution of its variation in the slip phases ΔF , as estimated from Eq. (3) with $\gamma = \gamma_c$ and at $T = 0$ [Figs. 4(a)–4(d)] and $T = 70$ K [Figs. 4(e)–4(h)]. The force F_x has an average value $|\overline{F_x}| = 0.288$ and 0.181 nN, respectively at $T = 0$, and 0.209 and 0.137 nN at 70 K, consistently with the fact that the static friction is reduced by thermal vibrations.

C. Route to chaos

For $\gamma \ll \gamma_c$ the tip path at $T = 0$ in 1D becomes chaotic [8]. This is also the case in 2D. Here it makes sense to describe the tip motion in the (x, v_x) plane of the 4D phase space, where $v_x = \dot{x}$. In Fig. 5(a) we first show a phase plot of the results obtained for $\gamma = \gamma_c$. The horizontal segments (see insets) correspond to the stick phases, where the tip slowly moves to the right following the spring support. When the shot point is reached, the unpinned tip explores the (x, v_x) plane along a curvy line and finally lands into another pinning site following a spiral pattern [25]. If the x coordinate of the tip is referred to the position $X = Vt$ of the support, the distinct attractors can be easily identified [5]. The plot of v_x as a function of $x - X$ or, equivalently, of the lateral force $F_x = k(x - X)$, is shown in Fig. 5(c). If $\gamma = \gamma_c$ the three landing points 4, 5, and 7 are easily recognized, but the same cannot be said for the 12 locations corresponding to $\gamma = 0.1\gamma_c$ [Figs. 5(b) and 5(d)]. In this case, the attractors are reached only after several windings initially embracing most or even all of them. We have also extracted the distribution of F_x in the slip phase by removing all data points with $v_x < 1 \mu\text{m/s}$ (Fig. 6). The three peaks in Fig. 6(a) correspond to the attractors in Fig. 3(c). The spurious peak highlighted by the arrow is caused by the winding ending into the main attractor 7. If $\gamma = 0.1\gamma_c$ the attempt of identifying the attractors by comparing the peaks in the histogram in Fig. 6(b) with the sequence in Fig. 3(f) is made difficult by the spreading of the shot points within the two spots highlighted by the red and orange arrows in Fig. 5(d). This gives rise to secondary attractors and corresponding satellite peaks highlighted in orange in Figs. 3(d) and 6(b).

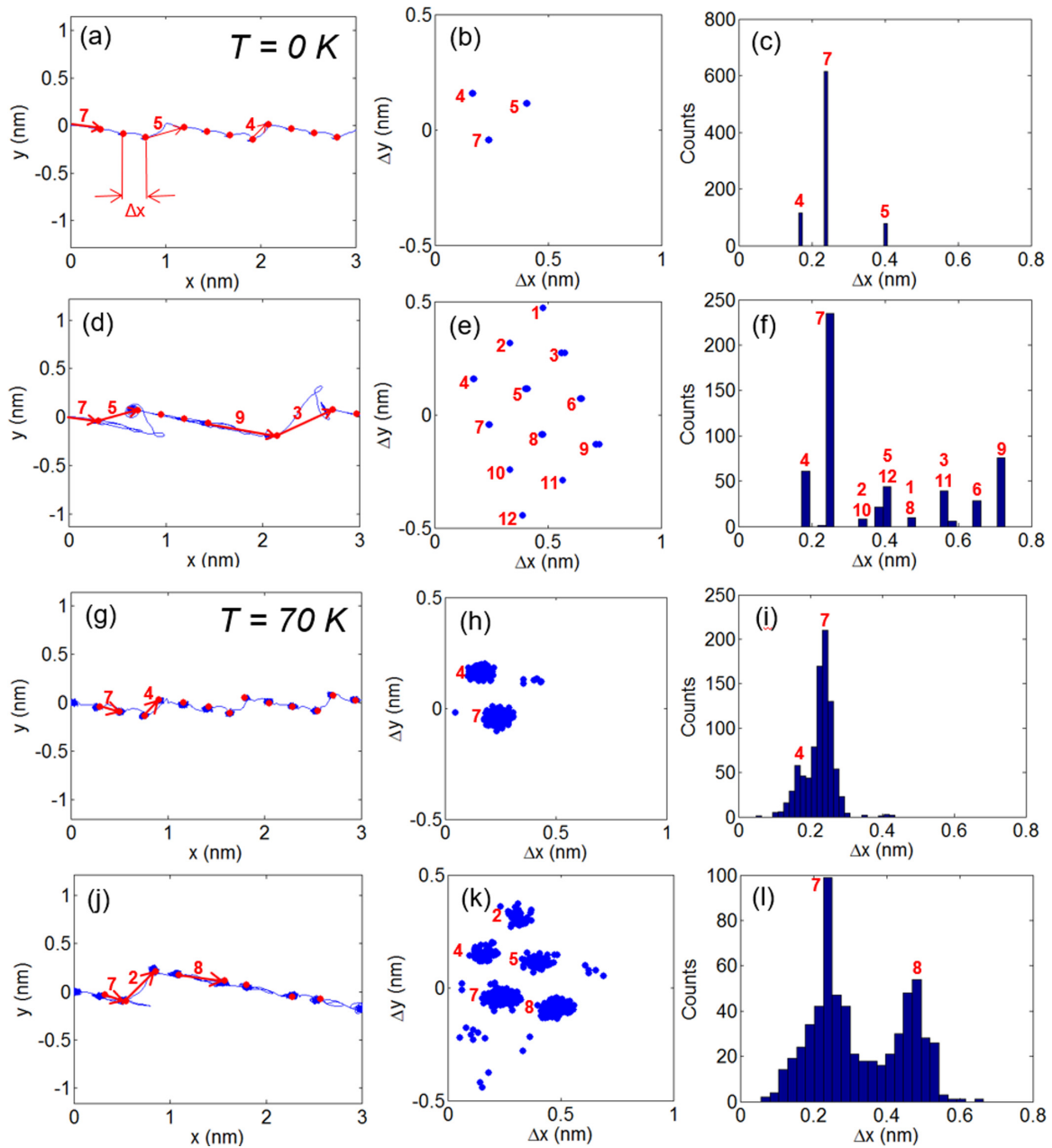


FIG. 3. (a) Tip path (in blue) over the potential defined by Eq. (1) rotated by an angle of -12° . The red dots correspond to the landing e-off points defined in the text. Stick-slip parameter: $\eta = 10$. Damping coefficient: $\gamma = \gamma_c$. (b) Attractor pattern as obtained from the change of the tip coordinates, Δx and Δy , between consecutive shot points. (c) Statistical distribution of Δx . (d)–(f) Same as (a)–(c) with $\gamma = 0.1\gamma_c$. (g)–(l) Same as (a)–(f) with a temperature $T = 70$ K.

D. Application to atomic force microscopy

Finally, we briefly discuss up to which point the previous analysis may help to interpret lateral force maps acquired using AFM. Figure 7 shows simulated maps of F_x and corresponding force drop histograms obtained after scanning 256 lines left to right and backward (not shown) on a $5 \times 5 \mu\text{m}^2$ area in the same conditions of Figs. 3(g) and 3(j). While the surface lattice can be clearly recognized when $\gamma = \gamma_c$, this is not the case when $\gamma = 0.1\gamma_c$ and only one crystallographic direction is clearly visible. When similar maps are acquired by AFM, the poor quality of images corresponding to Fig. 7(c) could be erroneously attributed to experimental

issues such as thermal drift. However, the previous discussion rather suggests that the force drop histograms, when compared with those simulated at different values of γ , could be efficiently used for an indirect estimation of the damping coefficient. An anticipation (based on single scan lines) is given by Fig. 8, where we have plotted the peak intensities for γ ranging from 0.1 to 2 times γ_c . We must also notice that Eq. (1) is the lowest order approximation for an interaction potential with hexagonal symmetry. Significant deviations can be expected not only due to the material properties of the sample surface, but also to the arrangement of the atoms forming the tip apex. This is well exemplified in the MD simulations accompanying friction anisotropy measurements on MoS_2 ,

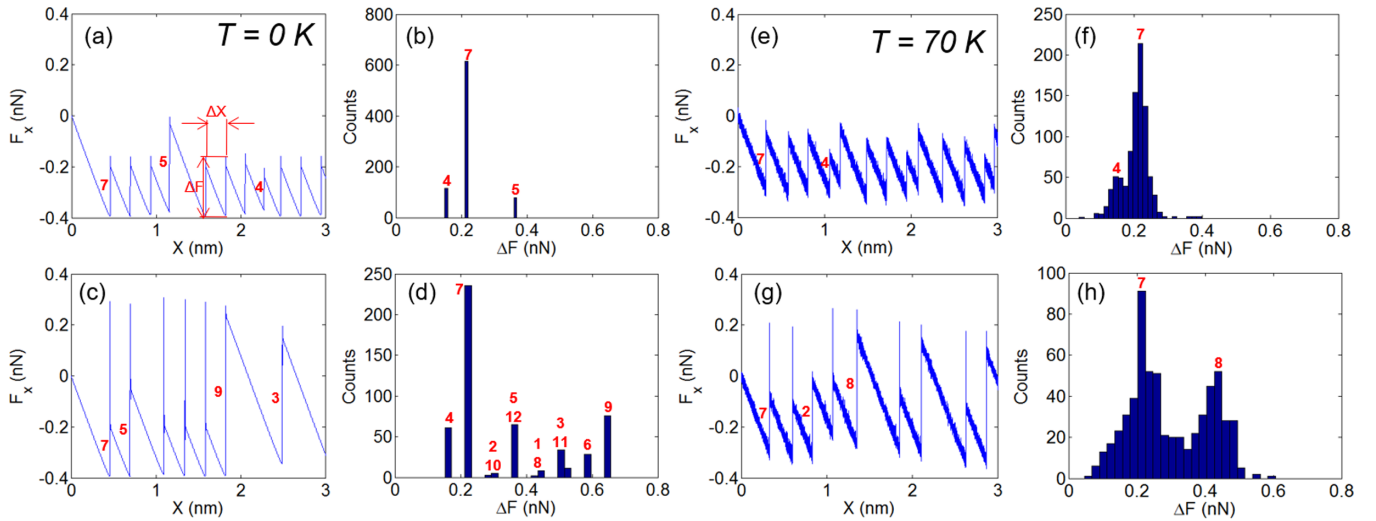


FIG. 4. (a) x component of the spring force as a function of the support position $X = Vt$. Damping coefficient: $\gamma = \gamma_c$. (b) Distribution of the force drop ΔF occurring in the slip phases. (c) and (d) Same as (a) and (b) with $\gamma = 0.1\gamma_c$. (e)–(h) Same as (a)–(d) with $T = 70\text{ K}$.

which were recently presented by Vazirisereshk *et al.* [26]. The sixfold symmetry of MoS_2 is significantly broken in the potential energy surface (PES) resulting from the simulations. As a next step, the analysis presented in this work could be repeated with the function $U_{\text{int}}(x, y)$ obtained by 2D Fourier

expansion of a PES obtained in a similar way with different orders of approximation.

IV. CONCLUSION

In summary, we have investigated how the stick-slip experienced by a sharp tip elastically driven on a hexagonal crystal lattice is influenced by the damping coefficient and the temperature for an arbitrary scan direction and selected values of those parameters. The effect of γ can be recognized in the histogram of the force drops accompanying the stick-slip, which could be directly compared with analogous histograms obtained from AFM friction measurements. The sliding direction determines the position of the peaks in

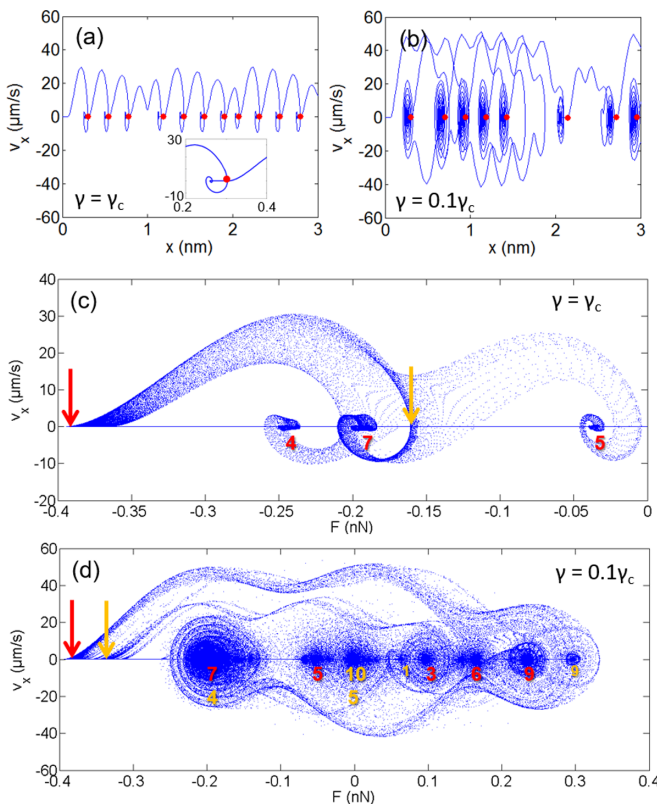


FIG. 5. Pathways in the (x, v_x) subspace at $T = 0\text{ K}$ for $\eta = 10$ and (a) $\gamma = \gamma_c$, (b) $\gamma = 0.1\gamma_c$. The inset highlights the stick phase at the first landing site. (c) and (d) Pathways corresponding to (a) and (b) with the spring force $F = k(x - X)$ in lieu of x (for sake of clarity only data points at time intervals of $1\ \mu\text{s}$ have been plotted).

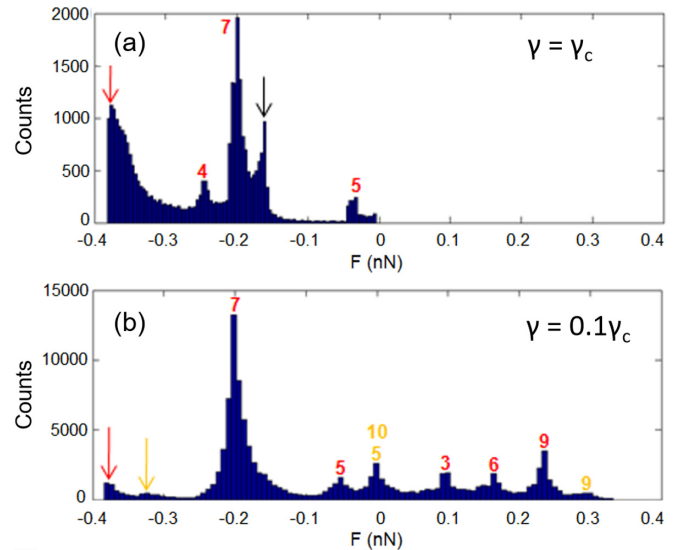


FIG. 6. (a) and (b) Histograms of the spring force (in the slip phase) as obtained from the data points in Figs. 5(c) and 5(d). Red and orange numbers label the force values at the end of the slips starting with the values in the regions indicated by the arrows of the same colors.

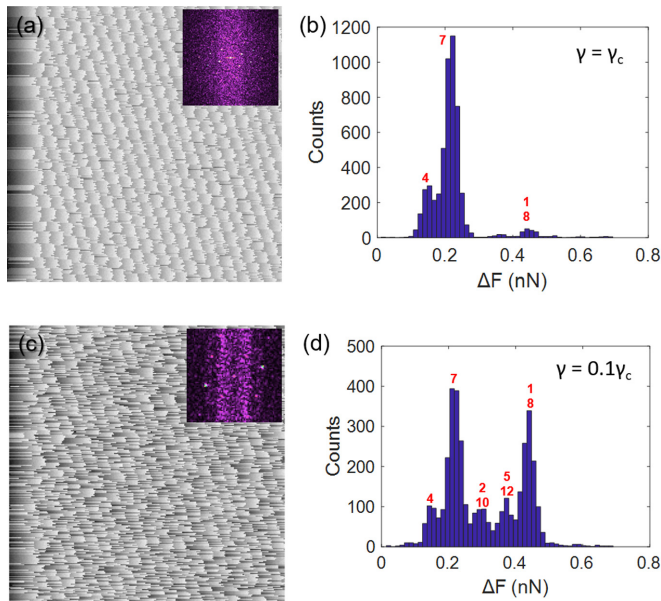


FIG. 7. (a) Simulated lateral force map (including FFT) and (b) force drop distribution corresponding to $T = 70$ K, $\eta = 10$, $\alpha = 12^\circ$, and $\gamma = \gamma_c$. (c) and (d) Same with $\gamma = 0.1\gamma_c$.

the histogram, provided that the spring constant is known. The damping coefficient changes the number of neighbor locations accessible through a slip and, consequently, the number and intensity of the histogram peaks. In doing that, one has to consider that this scenario is considerably influenced by the temperature. Thermal vibrations limit the occurrence of long slips, and broaden the width of the peaks, merging minor ones in the tails of the main ones. As a next step, a systematic investigation of force drops histograms at different values of γ and T , including empirical fitting equations, will be crucial for

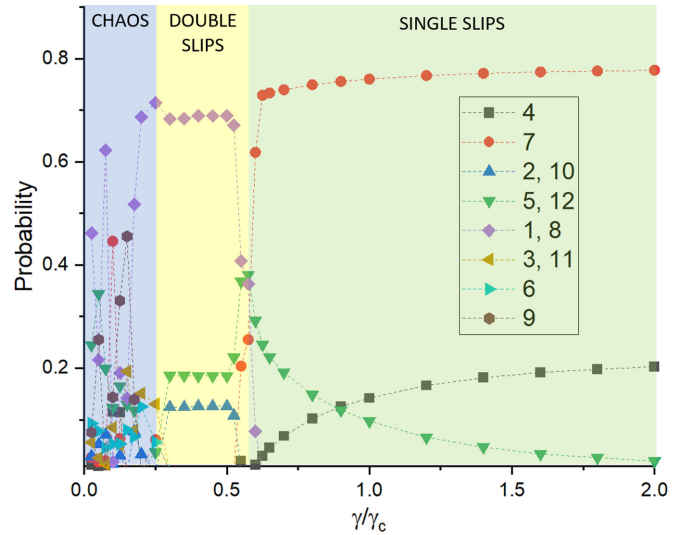


FIG. 8. Damping coefficient dependent slip probabilities of the possible landing sites on the hexagonal potential when $T = 0$ K, $\eta = 10$, and $\alpha = 12^\circ$.

accurate estimations of the damping coefficient from AFM-based friction experiments.

For the aforementioned reasons, a comprehensive analysis should include measurements at cryogenic temperatures, a possibility which was recently demonstrated in standard contact mode at 30 K by Wang *et al.* [27] and, indirectly, with the pendulum configuration adopted by Kisiel *et al.* at 5 K. [28].

ACKNOWLEDGMENTS

This work was funded with the support of the Deutsche Forschungsgemeinschaft Project DFG GN 92/16-1. The Strategic Program Excellence Initiative at the Jagiellonian University 'SciMat' (Grant No. U1U/P05/NO/01.05) is gratefully acknowledged by E.G.

- [1] J. Y. Park and M. Salmeron, *Chem. Rev.* **114**, 677 (2014).
- [2] B. N. J. Persson, *Sliding Friction: Physical Principles and Applications* (Springer, Heidelberg, 1998).
- [3] G. Witte, K. Weiss, P. Jakob, J. Braun, K. L. Kostov, and C. Wöll, *Phys. Rev. Lett.* **80**, 121 (1998).
- [4] S. Maier, Y. Sang, T. Filleter, M. Grant, R. Bennowitz, E. Gnecco, and E. Meyer, *Phys. Rev. B* **72**, 245418 (2005).
- [5] W. G. Conley, A. Raman, and C. M. Krousgrill, *J. Appl. Phys.* **98**, 053519 (2005).
- [6] Y. Dong, D. Perez, A. F. Voter, and A. Martini, *Tribol. Lett.* **42**, 99 (2011).
- [7] M. Evstigneev and P. Reimann, *Phys. Rev. B* **87**, 205441 (2013).
- [8] E. Gnecco, R. Roth, and A. Baratoff, *Phys. Rev. B* **86**, 035443 (2012).
- [9] R. Roth, T. Glatzel, P. Steiner, E. Gnecco, A. Baratoff, and E. Meyer, *Tribol. Lett.* **39**, 63 (2010).
- [10] A. Schirmeisen, L. Jansen, and H. Fuchs, *Phys. Rev. B* **71**, 245403 (2005).
- [11] Q. Yao and Q. Li, *Tribol. Lett.* **64**, 31 (2016).
- [12] D. W. van Baarle, S. Y. Krylov, M. E. S. Beck, and J. W. M. Frenken, *Tribol. Lett.* **67**, 15 (2019).
- [13] S. N. Medyanik, W. K. Liu, I. H. Sung, and R. W. Carpick, *Phys. Rev. Lett.* **97**, 136106 (2006).
- [14] L. Agmon, I. Shahar, D. Yosufov, C. Pimentel, C. M. Pina, E. Gnecco, and R. Berkovich, *Sci. Rep.* **8**, 4681 (2018).
- [15] S. Skuratovsky, L. Agmon, and R. Berkovich, *Tribol. Lett.* **68**, 113 (2020).
- [16] S. Skuratovsky, L. Agmon, E. Gnecco, and R. Berkovich, *Friction* (2022), doi: 10.1007/s40544-021-0590-5.
- [17] C. Lee, Q. Li, W. Kalb, X. Z. Liu, H. Berger, R. W. Carpick, and J. Hone, *Science* **328**, 76 (2010).
- [18] P. Steiner, R. Roth, E. Gnecco, A. Baratoff, S. Maier, T. Glatzel, and E. Meyer, *Phys. Rev. B* **79**, 045414 (2009).
- [19] M. P. Allen and D. J. Tildesley, *Computer Simulation of Liquids* (Clarendon, Oxford, 1990).
- [20] A. Socoliuc, R. Bennowitz, E. Gnecco, and E. Meyer, *Phys. Rev. Lett.* **92**, 134301 (2004).

- [21] K. Johnson and J. Woodhouse, *Tribol. Lett.* **5**, 155 (1998).
- [22] E. Gnecco, *Europhys. Lett.* **91**, 66008 (2010).
- [23] P. Steiner, R. Roth, E. Gnecco, A. Baratoff, and E. Meyer, *Phys. Rev. B* **82**, 205417 (2010).
- [24] L. Jansen, H. Hölscher, H. Fuchs, and A. Schirmeisen, *Phys. Rev. Lett.* **104**, 256101 (2010).
- [25] G. Djuidjé Kenmoé, A. Kenfack Jiotsa, and T. C. Kofané, *Eur. Phys. J. B* **70**, 353 (2009).
- [26] M. R. Vazirisereshk, K. Hasz, R. W. Carpick, and A. Martini, *J. Phys. Chem. Lett.* **11**, 6900 (2020).
- [27] W. Wang, D. Dietzel, and A. Schirmeisen, *Sci. Adv.* **6**, eaay0165 (2020).
- [28] M. Kisiel, O. O. Brovko, D. Yildiz, R. Pawlak, U. Gysin, E. Tosatti, and E. Meyer, *Nat. Commun.* **9**, 2946 (2018).